ACS OMEGA

Open Access

http://pubs.acs.org/journal/acsodf

Article

Hydrothermal Synthesis and Electrochemical Performance of the $Ce_2Mo_3O_{12}/MoS_2/C$ Composite as Anode Material for Lithium-Ion Batteries

Wei Liu,* Jingbo Zhang, Dongsheng Fan, Yaozong Lu, Linping Fu, Longhua Zhang, and Ming Li

Cite This: *ACS Omega* 2025, 10, 18539−18551

Read Online

ACCESS | Metrics & More | Article Recommendations

ABSTRACT: Rare earths are of significant benefit to the electrochemical performance, reliability, and safety of batteries. The integration of rare earth elements into MoS_2 anode materials holds promise for enhancing the cycling stability of batteries during charging and discharging cycles. In this work, a nanoflower-like composite of $Ce_2Mo_3O_{12}/MoS_2/C$ was synthesized as an anode material by an enhanced hydrothermal method. The experimental results showed that the incorporation of carbon resulted in a more sophisticated flower-like structure of the material. The annealing process has little effect on the morphology and crystal structure of the $Ce_2Mo_3O_{12}/MoS_2/C$ composite. After being annealed at 500 °C for 2 h, the $Ce_2Mo_3O_{12}/MoS_2/C$ composite exhibited remarkable cycling stability as an anode material for lithium-ion batteries (LIBs). The initial discharge capacity at a current density of 500 mA g^{-1} was 747.98 mAh g^{-1}, while the discharge capacity after 200 cycles exhibited a capacity retention rate of 77.34%. The results demonstrate the potential of this material for energy storage applications and provide an alternative to the rational design of related materials.

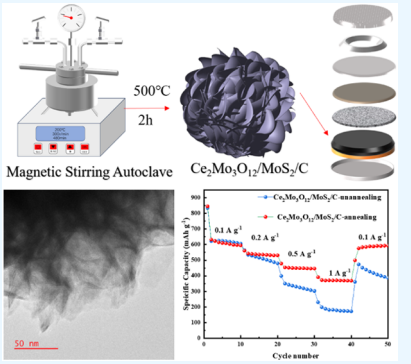

1. INTRODUCTION

Solar and wind energy can reduce carbon emissions from fossil fuels, aiding in global carbon peaking and neutrality goals. However, their discontinuous supply due to natural factors hampers efficient utilization. Thus, developing reliable and efficient energy storage systems to store electricity from these sources is crucial for their practical application.[1,2] Lithium-ion batteries (LIBs) have garnered significant attention owing to their distinctive advantages, including high energy density, extended cycle lifespan, and minimal self-discharge capability.[3,4] As a key component, the anode properties greatly influence the LIB performance. Industrial graphite electrodes, limited by low theoretical capacity and poor electrolyte compatibility, hinder their use in high-energy-density LIBs. Molybdenum disulfide (MoS_2), with its high theoretical capacity (670 mAh g^{-1}), large surface area, excellent electrochemical activity, and low cost, emerges as a promising anode material for LIBs.[4−9] Nevertheless, poor electrical conductivity and large volume expansion during the charging and discharging processes have impeded the commercialization of MoS_2 as an anode material for LIBs. As the most effective strategies, nanocrystallization of MoS_2 and the incorporation of MoS_2 with other compounds were employed to address the aforementioned shortcomings.[10−13]

The nanostructured design of the MoS_2 material has the potential to significantly provide more active reaction sites, shorten the diffusion pathway, and enhance the diffusion efficiency of lithium ions and electrons during the charging and discharging processes. In recent years, nanosized MoS_2 with various morphologies has been successfully synthesized, including two-dimensional nanosheets[3,10] and three-dimensional nanospheres.[7,14] In addition to regulating the morphology of MoS_2, incorporation with other materials is also an effective approach to improve the electrochemical performance of MoS_2-based anode materials. For example, the incorporation of carbon materials,[3,14−16] MXene,[17] and transition metal oxides[9,18] with MoS_2 has been demonstrated to mitigate the structural collapse of anode materials that occurs during the charge/discharge reactions.

As a novel functional material, rare earth element compounds exhibit stable energy level structure, catalysis, and other superior properties, rendering them suitable for a multitude of applications in the field of new energy.[19−21] Cheng et al.[22] synthesized CeO_2 mesoporous microspheres comprised of nanoparticles. The integrated structure of the CeO_2 electrode endows it with a notable lithium storage capacity and excellent rate performance. Wen et al.[23] have

Received: December 10, 2024
Revised: March 15, 2025
Accepted: April 28, 2025
Published: May 2, 2025

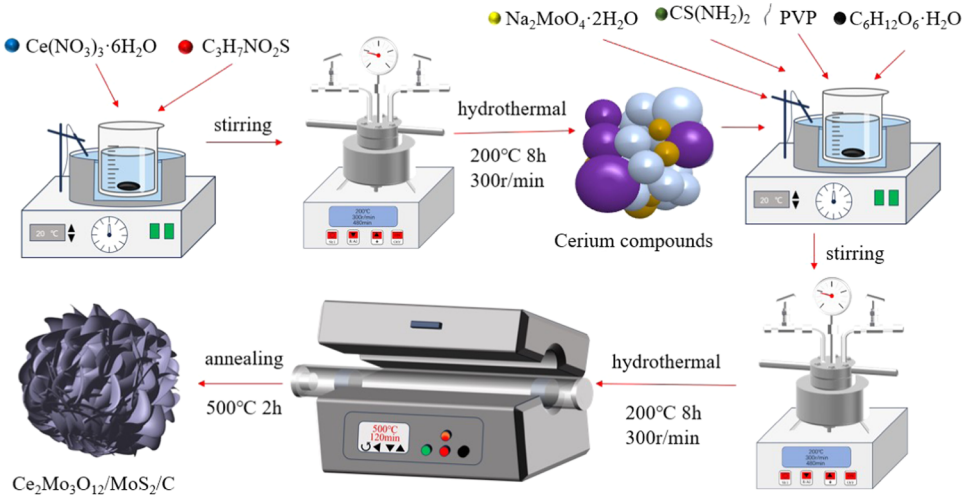

Figure 1. Schematic illustration of the CMC composite preparation.

developed a novel nitrogen-doped carbon fiber structure embedded in hollow cerium oxide spheres (CeO_2@NCF). The hollow spherical structure of CeO_2, characterized by abundant vacancies, offers additional catalytic sites for lithium-ion aggregation and transport. Due to the synergistic effect between CeO_2 and NCF, the anode material demonstrates high capacity and excellent cycle stability, achieving a discharge capacity of 450.8 mAh g^{-1} after 500 cycles at a current density of 1 A g^{-1}.

Doping cerium into molybdenum disulfide (MoS_2) can adjust its structure and boost the lithium storage capacity. Cerium, often used as a dopant in metal-ion batteries, helps reduce internal impedance during discharge.[24] Santhoshkumar et al.[25] synthesized a cerium molybdate microsphere composite ($Ce_2Mo_5O_{16}$) with a microsheet structure by the hydrothermal method. The large specific surface area of the composite enhances the energy storage capacity. Additionally, the network of orderly flakes creates a myriad of wide-open spaces, which facilitate the penetration of electrolyte ions and enable swift electron transport. Feng et al.[26] prepared CNT-MoS_2/CeO_2 nanocomposites via a straightforward hydrothermal process. The initial discharge capacity was 1373.4 mAh g^{-1} at a current density of 0.1 C, and after 200 cycles, the capacity retained was 933.9 mAh g^{-1}. The active site of CeO_2 inhibits dissolution and alleviates the shuttle effect of the polysulfide. In addition, the incorporation of carbon nanotubes provides a buffer space for the volume expansion of the electrode that occurs during the charge/discharge cycles.

In general, the rare earth elements are of great importance to enhance the stability of batteries.[27,28] The incorporation of rare earth elements with MoS_2 will address the inherent issues of high volume expansion during the charging and discharging process. In this study, an enhanced hydrothermal method[16,29] was employed to synthesize the $Ce_2Mo_3O_{12}/MoS_2$ composite (CM). In order to enhance the electrical conductivity of the samples, carbon materials are incorporated into the synthesis procedure to form the $Ce_2Mo_3O_{12}/MoS_2$/C composite (CMC). The composite material displayed a distinctive morphology structure comprising nanoflower-like stacking, which was formed by the aggregation of nanosheets. The flaky nanoflowers exhibited a larger specific surface area and much exposure of active sites, which enhanced the surface area and reaction efficiency of the electrode reaction, thereby improving the discharge capacity of the material. Furthermore, this unique structure can alleviate the volume changes of the material during cycling, bolster the structural stability of the anode material, and consequently enhance the cycling stability of the battery.

2. EXPERIMENTAL SECTION

2.1. Synthesis of the $Ce_2Mo_3O_{12}/MoS_2$/C Composite. The typical experimental procedure is depicted in Figure 1. All reagents were of analytical grade and were used without further purification. A total of 1.15 g of cerium nitrate hexahydrate ($Ce(NO_3)_3·6H_2O$, China) and 1.5 g of L-cysteine ($C_3H_7NO_2S$, China) were dissolved in deionized water. After being completely dissolved, the solution was transferred to a 200 mL modified polyethylene tetrafluoride (PTFE) lined micro magnetic stirring autoclave at 200 °C for 8 h with a rotation speed of 300 rpm. Then, the precipitation was centrifuge washed using deionized water and anhydrous ethanol alternately 4 times and then dried at 60 °C in a vacuum oven for 12 h. The as-prepared cerium compound was dispersed in 80 mL of deionized water with 1.95 g of sodium molybdate ($Na_2MoO_4·2H_2O$, China), 3.66 g of thiourea ($CS(NH_2)_2$, China), 0.1 g of polyvinylpyrrolidone (PVP), and 1 g of glucose ($C_6H_{12}O_6·H_2O$, China). After completely dissolving, a solution of dilute sulfuric acid (Vol. 20%) was added to adjust the solution pH value to 2. Finally, the solution was transferred to the same autoclave and reacted under the identical hydrothermal conditions as previously described. The products were centrifugally washed and dried to obtain a $Ce_2Mo_3O_{12}/MoS_2$/C composite (CMC). As heat treatment in an vital step for many of the synthesis procedure,[30] the CMC samples were then annealed at 500 °C under an argon atmosphere for 2 h. Sodium molybdate and thiourea were used to synthesize pure MoS_2 material, and the $Ce_2Mo_3O_{12}/MoS_2$ composite (CM) was synthesized without glucose under identical conditions for reference.

2.2. Characterization of the $Ce_2Mo_3O_{12}/MoS_2$/C Composite. The crystal structure of the samples was examined through the utilization of various advanced techniques. Specifically, X-ray diffraction (XRD, Germany), a field emission scanning electron microscope (FESEM, Japan), and a high-resolution transmission electron microscope (HRTEM, Japan) were employed. To determine the

https://doi.org/10.1021/acsomega.4c11155
ACS Omega 2025, 10, 18539−18551

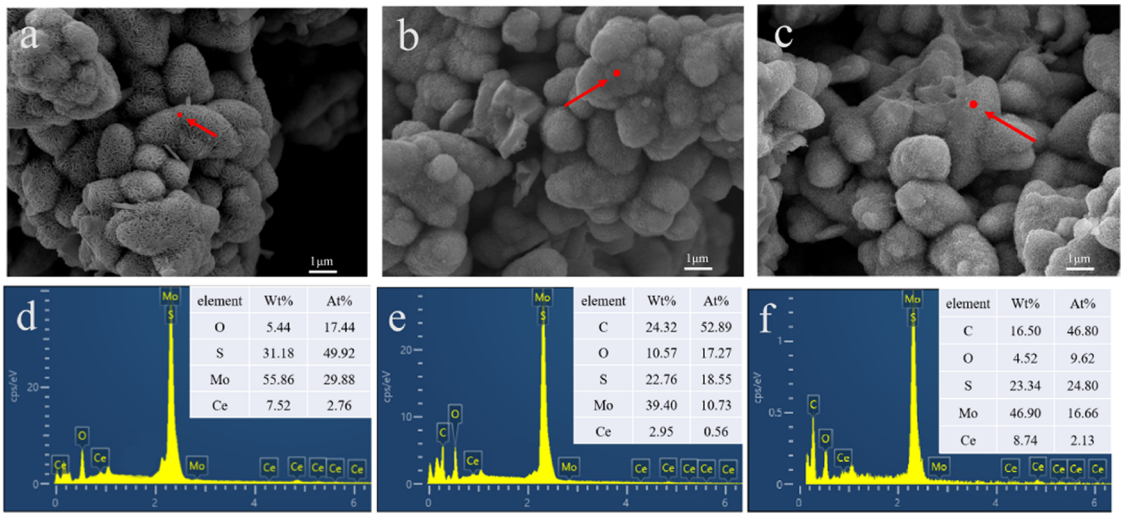

Figure 2. FESEM images of the CM (a), CMC (b), and CMC after annealing (c). EDS images of the CM (d), CMC (e), CMC after annealing (f).

composition and specific content of the specimens, an energy-dispersive spectrometer (EDS) was used. The BET tests were carried out with a surface area and pore size distribution analyzer (BELSORP-max II, Japan). Additionally, an X-ray photoelectron spectrometer (XPS) equipped with an Al Kα X-ray source was utilized for a comprehensive analysis of the elemental composition and valence states of the elements present in the specimens.

2.3. Electrochemical Measurements. Prior to further processing, the samples were thoroughly mixed and ground with acetylene black and polyvinylidene fluoride. Subsequently, a quantity of 20 drops of *N*-methylpyrrolidone (NMP) was added to achieve a slurry with moderate viscosity. This slurry was then evenly spread onto the unpolished surface of pristine copper foils and served as the anode material. The assessment of the capacities and cycling characteristics of the prepared samples involved the use of CR2032 buckle cells, which were assembled in an argon-filled glovebox, with a lithium sheet serving as the counter electrode. The electrochemical behaviors, including cyclic voltammetry (CV) and electrochemical impedance spectroscopy (EIS), were conducted on the CHI660E Electrochemical Workstation. Additionally, the CT2001A button battery test system was employed to evaluate the charge−discharge cycling performance and rate capability of the samples.

3. RESULTS AND DISCUSSION

3.1. Crystal Structure, Morphology, and Composition. The FESEM images of the as-prepared CM and CMC composites are presented in Figure 2a−c. The synthesized CM composite (as illustrated in Figure 2a) exhibits a nanoflower-like structure, formed by the aggregation of nanosheets. The addition of glucose results in a more refined structure (Figure 2b). During the hydrothermal process, glucose was carbonized to form gray carbon micelles that serve as heterogeneous nucleation sites for MoS_2. Additionally, the agitation of the system facilitates the coating of gray carbon micelles on the surface of the nucleated MoS_2 nanocrystals, thereby reducing the specific surface energy of the nano-MoS_2 and inhibiting the further stacking aggregation of MoS_2.[16] The morphology of the as-prepared CMC sample after annealing (Figure 2c) exhibits minimal alteration in comparison to the unannealed counterpart, displaying a flaky nanoflower-like stacking structure.

Figure 2d−f illustrates the EDS spectra and the elemental content of the as-prepared CM samples and the CMC composite. The analysis reveals that the product is predominantly composed of molybdenum, sulfur, carbon, oxygen, and cerium. The Au element is introduced during the conductive coating stage, for improving the electrical conductivity of the material and enhancing the imaging effect. Furthermore, the EDS energy spectrum of the CMC specimen after annealing displays a reduction in the mass fraction of C and O elements in comparison to that of the samples without annealing. This can be attributed to the oxidation of carbon with adsorbed oxygen on its surface during the high-temperature process, which is accompanied by an increase in the mass fraction of Mo, S, and Ce elements.

Figure 3 depicts the X-ray diffraction (XRD) patterns of the as-prepared CM and CMC composite. It was observed that the addition of glucose had no significant impact on the diffraction peak position of the sample, indicating that the main components of the material are $Ce_2Mo_3O_{12}$ and MoS_2. However, the peak intensity of the sample is enhanced with

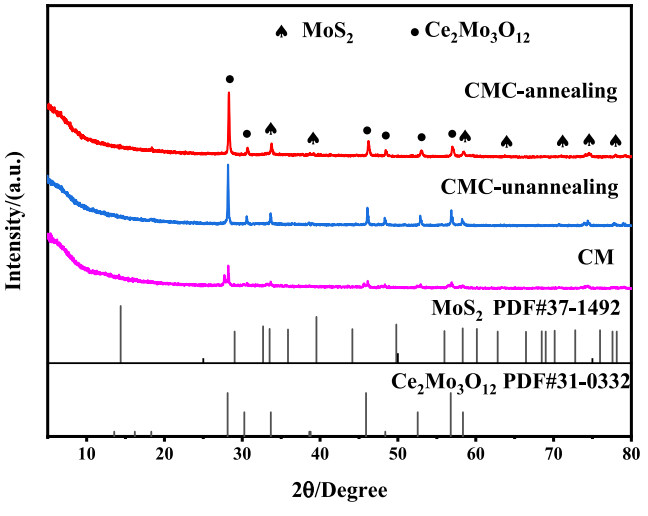

Figure 3. XRD patterns of the CM, CMC, and CMC after annealing.

https://doi.org/10.1021/acsomega.4c11155
ACS Omega 2025, 10, 18539−18551

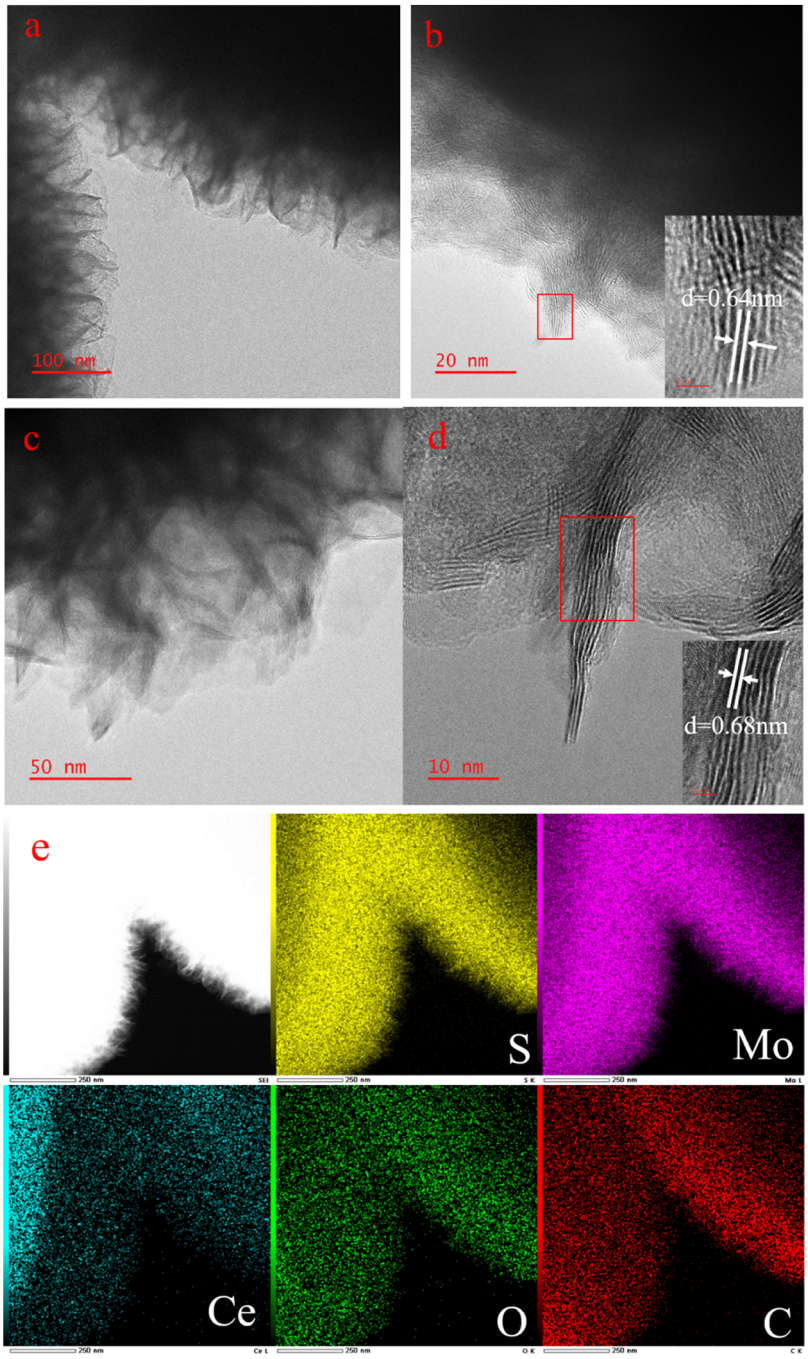

Figure 4. HRTEM images of the CMC before annealing (a, b). HRTEM images of the CMC after annealing (c, d). Elemental mapping images of Mo, S, Ce, O, and C for the CMC (e).

the addition of glucose. This is attributed to the carbon source generated by the decomposition of glucose in the hydrothermal process, which contributes to the growth of nanosheets, and enhances the diffraction peak intensity of the material.[29] After annealing at 500 °C, the diffraction peak of the CMC sample exhibited little significant difference, indicating that the annealing treatment did not result in any notable alteration to the primary composition of the samples.

The high-resolution transmission electron microscopy images of the CMC composite before and after annealing at 500 °C are shown in Figure 4. As illustrated in Figure 4a,c, the particle size distribution is relatively uniform, suggesting that carbon is distributed homogeneously in the powder. EDS mapping results for the unannealed samples are shown in Figure 4e, which revealed that the composite material is primarily composed of molybdenum disulfide, with carbon uniformly distributed on the surface of the material. The cerium element is predominantly located in the central part of the sample, and a few cerium is also attached to the molybdenum disulfide nanosheets at the edges. Furthermore, the images provide compelling evidence for the growth mechanism of the sample, where cerium molybdate is initially formed, and molybdenum disulfide nanosheets subsequently grow and encapsulate the surface of the cerium molybdate. This structure has the beneficial effect of mitigating the volume change of the material during the charge/discharge processes,

https://doi.org/10.1021/acsomega.4c11155
ACS Omega 2025, 10, 18539−18551

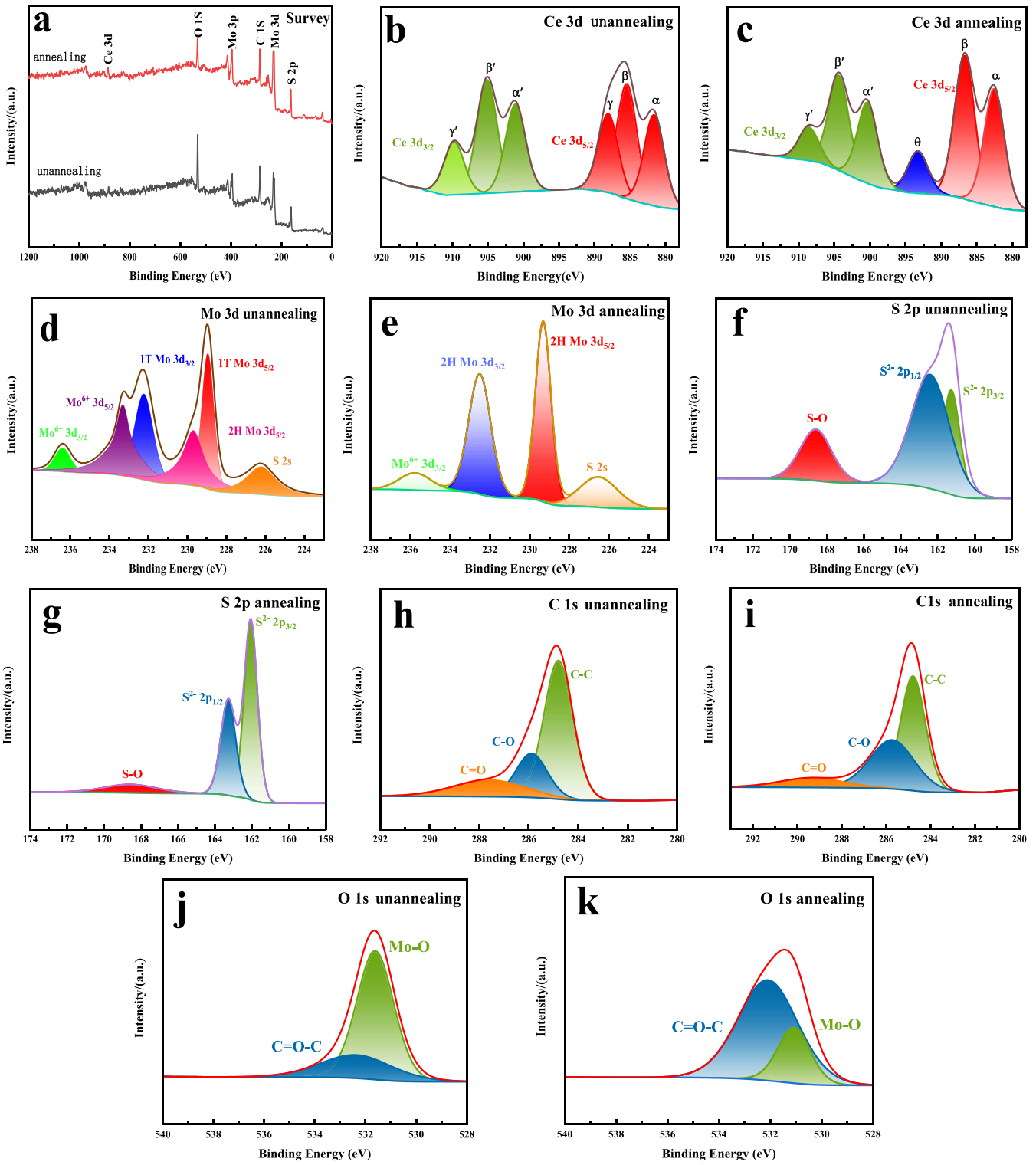

Figure 5. XPS spectra of CMC materials before and after annealing ((a) survey spectra; (b) Ce 3d unannealing; (c) Ce 3d annealing; (d) Mo 3d unannealing; (e) Mo 3d annealing; (f) S 2p unannealing; (g) S 2p annealing; (h) C 1s unannealing; (i) C 1s annealing; (j) O 1s unannealing; (k) O 1s annealing).

thereby enhancing the cycle stability of the material. A comparison of Figure 4b,d reveals that the annealing treatment results in a notable enhancement in the continuity and order of the nanosheet lattice stripes, accompanied by an increase in the lattice spacing from 0.64 nm before annealing to 0.68 nm after annealing, which are both larger than those of the pristine MoS_2. The enlarged lattice space is conducive to lithium-ion embedding and de-embedding. These findings indicate that annealing at 500 °C can effectively remove internal defects in the material, avoid the particles smashing due to the stress concentration of the material during the cycling process, and thereby enhance the material cycle stability.

Figure 5 illustrates the X-ray photoelectron spectroscopy (XPS) spectra of CMC before and after annealing at 500 °C.

https://doi.org/10.1021/acsomega.4c11155
ACS Omega 2025, 10, 18539−18551

Figure 5a depicts the survey spectrum of the as-prepared CMC composite, which includes the elements Ce, Mo, S, C, and O. Figure 5b,c shows the refined Ce 3d spectra before and after annealing, which both exhibit six distinctive peaks. Before annealing, these peaks located at 881.6, 885.4, 888.1, 901.1, 905.2, and 909.8 eV, which were represented by α, β, γ, α', β', and γ', respectively. The peaks β and β' are attributed to Ce^{3+} $3d_{5/2}$ and Ce^{3+} $3d_{3/2}$, α and γ correspond to Ce^{4+} $3d_{5/2}$, α' and γ' are assigned to Ce^{4+} $3d_{3/2}$, respectively. These distinctive peaks indicate that Ce is present in the composite in a multivalent valence state. After annealing, the characteristic peaks for α, β, α', β', and γ' shift to 882.6, 886.7, 901.6, 905.7, and 911.3 eV, respectively. Furthermore, the characteristic peak of γ was eliminated and replaced by a θ characteristic peak at 893.4 eV, which corresponds to the satellite peaks of Ce.[31−35] The interaction between cerium and glucose results in the transformation of Ce^{4+} into Ce^{3+}, which in turn leads to the generation of oxygen vacancies and thus enhances the electrochemical activity of the material. After calcination, the area of the Ce^{4+} peak decreases while the area of the Ce^{3+} peak increases, indicative of a relatively higher Ce^{3+} content, which improves the electrochemical activity.[36] Figure 5d,e presents the Mo 3d spectra of the element before and after annealing. The two main characteristic peaks at 228.9 eV (Mo $3d_{5/2}$) and 232.3 eV (Mo $3d_{3/2}$) are attributed to Mo^{4+} in the 1 T phase MoS_2, while the peak that appeared at 229.7 (Mo $3d_{5/2}$) is indexed to Mo^{4+} in the 2 H phase MoS_2. The energy level splitting of Mo 3d leads to a typical difference in binding energy between the two spin−orbit split peaks of 3.15 eV. However, for metallic phase Mo-base material, the difference in binding energy is slightly larger. Given the metallic nature of 1T-phase molybdenum disulfide, the difference in binding energy between its two peaks is accordingly larger, corresponding to the observed peaks of Mo^{4+} in the 1T phase in the Figure 5d,e. The Mo^{4+} $3d_{3/2}$ peak from the 2H-phase molybdenum disulfide should theoretically be located at 232.9 eV. However, at this position, due to the relatively low content of Mo^{4+} in the 2H phase, it may be obscured by intense peak noise, making it impossible to fit the Mo^{4+} $3d_{3/2}$ peak accurately. The peaks at 236.4 and 233.3 eV are attributed to Mo^{6+} $3d_{3/2}$ and Mo^{6+} $3d_{5/2}$, respectively.[37−4142] The Mo^{6+} are mainly derived from $Ce_2Mo_3O_{12}$ present in the sample, with part of the Mo^{6+} potentially attributable to MoO_3, which can be formed by the surface oxidation of MoS_2. However, the presence of Mo^{6+} in the sample is predominantly in the form of MoO_4^{2-} rather than MoO_3, which results in a slight shift in the peak position of Mo^{6+}. In addition, the minor peak at 226.2 eV corresponds to S 2s.[41] After annealing, the 1T phase of metastable molybdenum disulfide converts entirely to the 2H phase of molybdenum disulfide at high temperatures due to its inherent instability. As a result, the peaks corresponding to the 1T phase of molybdenum disulfide disappear completely, while the peaks of the 2H phase intensify. The peaks of Mo^{4+} $3d_{5/2}$ and Mo^{4+} $3d_{3/2}$ are observed at 229.3 and 232.5 eV, respectively. The peak at 235.8 eV corresponds to Mo^{6+} $3d_{3/2}$. Theoretically, the peak of Mo^{6+} $3d_{5/2}$ should be located at 232.6 eV. However, during the annealing process, most of the MoO_3 sublimates, leading to a reduction in the intensity of the Mo^{6+} peaks. Consequently, the Mo^{6+} $3d_{5/2}$ peak at this position is interfered with by the intense Mo^{4+} peak, making it impossible to fit accurately.[43−45] The small peak at 226.5 eV is attributed to S 2s.

Figure 5f,g illustrates the three distinctive peaks of S 2p present in the specimens before and after annealing. The peaks at 161.3 and 162.4 eV before annealing are attributed to S^{2-} $2p_{3/2}$ and S^{2-} $2p_{1/2}$, respectively.[12,24] The peak at 168.6 eV is attributed to the formation of sulfur oxides, which result from the oxidation of MoS_2 in the air.[46] After annealing, the intensity of the peak at 168.6 eV is significantly reduced, corresponding to enhancement of the characteristic peak of S^{2-} $2p_{3/2}$. This indicates that the S−O bond decomposes during the annealing process. The peaks of S^{2-} $2p_{3/2}$ and S^{2-} $2p_{1/2}$ shift to 162.1 and 163.3 eV, respectively.[47,48] The C 1s exhibited three characteristic peaks, as illustrated in Figure 5h,i. Prior to annealing, characteristic peaks at 284.8, 285.8, and 287.6 eV correspond to the C−C, C−O, and C═O bonds, respectively.[14,41,49] These bonds are attributed to the amorphous carbon derived from the decomposition of glucose. In contrast, Figure 5i depicts the C 1s spectrum of the samples after annealing. The three characteristic peaks at 284.8 285.7, and 289.3 eV correspond to the C−C, C−O, and C═O, respectively. The peak area of the C═O bond is diminished due to the decomposition of the C═O bond in the annealing procedure, leading to an increase in the intensity of the C−O bond. The O 1s spectra of the as-prepared CMC composite before and after calcination are shown in Figure 5j,k. Prior to annealing, the peaks at around 531.6 and 532.4 eV correspond to Mo−O and C═O−C, respectively.[50,51] After annealing, the two characteristic peaks are still evident, exhibiting a shift to 531.1 and 532.1 eV, respectively. However, during the high-temperature annealing process, the area of the Mo−O characteristic peak is attenuated due to the sublimation of MoO_3, which is accompanied by an increase in the intensity of the C═O−C characteristic peak.

BET tests were carried out by the surface area and pore size distribution analyzer and the resulting data were summarized in Table 1. It is shown that the CMC sample without annealing has a higher specific surface area (32.17 m^2 g^{-1}) than that of its annealed counterpart (29.80 m^2 g^{-1}). However, the disparity of the two samples is minimal, indicating little change in their morphology and structure, which is consistent with the FESEM observations (shown in Figure 2). The BET results show that the isothermal curve of CMC is of the typical type IV shape, with obvious H3-type hysteresis loops. These loops are indicative of the predominant mesoporous characteristics of CMC. Consequently, the CMC after annealing and the CMC prior to annealing are mesoporous materials, with the pore size of the former being larger (20.36 nm) than the latter (17.05 nm). The N_2 adsorption/desorption isotherm and pore size distribution of the two samples are shown in Figure 6a,b, respectively. As can be observed from the Figure 6, the adsorption and desorption curves of the CMC before and after annealing nearly coincide.

Table 1. BET Testing Results of the As-Synthesized Materials

sample	SA_{BET} (m^2 g^{-1})	pore volume (cm^3 g^{-1})	pore size (nm)
CMC after annealing	29.80	0.15	20.36
CMC	32.17	0.14	17.05

3.2. Synthesis Mechanism. Based on the above discussion regarding the characterization results of the samples,

https://doi.org/10.1021/acsomega.4c11155
ACS Omega 2025, 10, 18539−18551

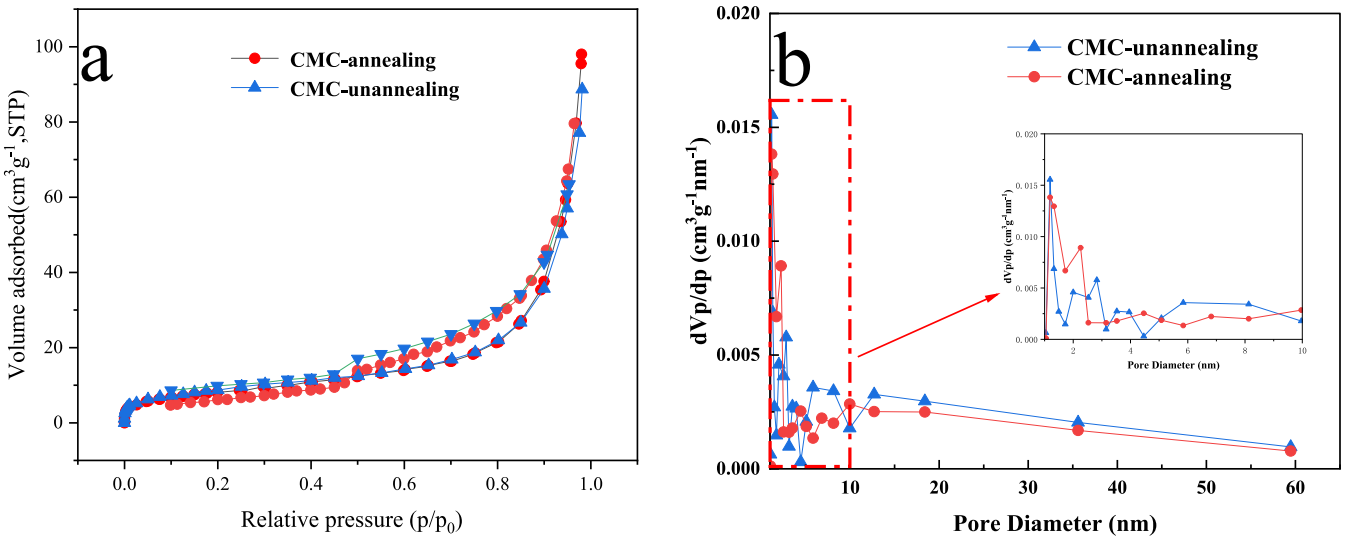

Figure 6. (a) N_2 adsorption/desorption isotherm and (b) the corresponding pore size distribution of the CMC composite.

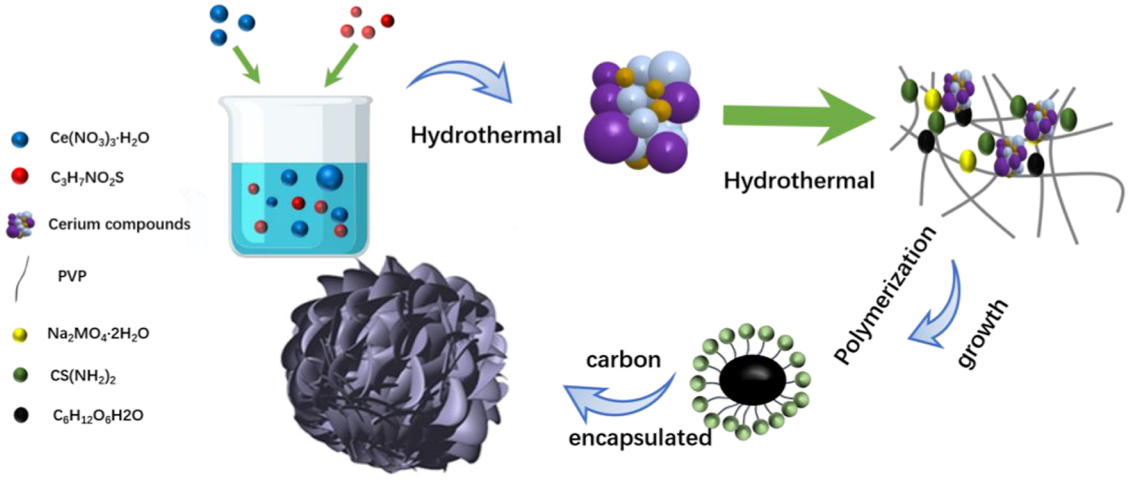

Figure 7. Illustration of synthesis mechanism for the CMC composite.

a hypothesized hydrothermal synthesis reaction mechanism of the product is proposed, as illustrated in Figure 7.

The final composite was prepared by two individual hydrothermal synthesis processes. In the first hydrothermal process, the product synthesized by the addition of cerium nitrate hexahydrate and L-cysteine is a mixed compound comprising Ce_2S_3, Ce_2O_3, and CeS_2.[52] At elevated temperatures and pressures, cerium ions hydrolyze to form Ce_2O_3, which is then reduced to Ce_2S_3 by H_2S, the decomposition product of L-cysteine. This process results in the generation of a minor quantity of CeS_2. The reaction mechanism can be described as follows

$$2Ce^{3+} + 3H_2O \rightarrow Ce_2O_3 + 6H^+ \quad (1)$$

$$2C_3H_7NO_2S + 5O_2 \rightarrow 2NH_3 + 2H_2S + 6CO_2 + 2H_2O \quad (2)$$

$$Ce_2O_3 + 3H_2S \rightarrow Ce_2S_3 + 3H_2O \quad (3)$$

$$2Ce_2O_3 + 8H_2S + O_2 \rightarrow 4CeS_2 + 8H_2O \quad (4)$$

In the following hydrothermal procedure, the cerium compound reacts with MoO_4^{2-} to yield $Ce_2Mo_3O_{12}$. Concurrently, MoO_4^{2-} reacts with thiourea, resulting in the formation of MoS_2. Subsequently, the CM composite is produced. The reactions that occur in the second hydrothermal process are described as follows

$$Na_2MoO_4 \rightarrow 2Na^+ + MoO_4^{2-} \quad (5)$$

$$CS(NH_2)_2 + 2H_2O \rightarrow 2NH_3 + H_2S + CO_2 \quad (6)$$

$$4MoO_4^{2-} + 9S^{2-} + 24H^+ \rightarrow 4MoS_2 + SO_4^{2-} + 12H_2O \quad (7)$$

$$Ce_2O_3 + 3MoO_4^{2-} + 6H^+ \rightarrow Ce_2Mo_3O_{12} + 3H_2O \quad (8)$$

$$Ce_2S_3 + 3MoO_4^{2-} + 6H^+ \rightarrow Ce_2Mo_3O_{12} + 3H_2S \quad (9)$$

$$2CeS_2 + 3MoO_4^{2-} + 8H^+ \rightarrow Ce_2Mo_3O_{12} + 4H_2S \quad (10)$$

In the initial stage of the second hydrothermal process, $Ce_2Mo_3O_{12}$ is first formed in the solution. Subsequently, glucose is carbonized at 180 °C or higher to produce gray carbon micelles, and MoS_2 forms with a uniform nanosheets structure. Subsequently, the carbon and MoS_2 formed as a uniform composite, and coated on the surface of $Ce_2Mo_3O_{12}$ to generate uniformly dispersed nanoflower-like CMC

https://doi.org/10.1021/acsomega.4c11155
ACS Omega 2025, 10, 18539−18551

composite material. The unique structure, in addition to the improved electrical conductivity afforded by carbon, will favor stable cycling performance and excellent capacity retention.

3.3. Electrochemical Performance. The pristine MoS_2, CM, unannealed CMC, and annealed CMC were assembled into button batteries, respectively. The charge−discharge cyclic performance of the material is shown in Figure 8. The initial discharge-specific capacities of the pristine MoS_2, CM, CMC (unannealed), and CMC (annealed) at a current density of 500 mA g^{-1} are 673.1, 542.9, 796.4, and 747.98 mAh g^{-1}, respectively. The CMC electrode after annealing maintained the discharge capacity of 411.60 mAh g^{-1} over 200 cycles with an excellent capacity retention of 77.34% (in comparison to the second cycle), which is higher than that of the CMC composite electrodes without annealing. The second discharge capacity exhibited a notable decline, which can be attributed to the generation of the solid electrolyte interface (SEI) film formed during the first discharge−charge cycle. Subsequently, the capacity demonstrates a gradual and consistent evolution, which may be indicative of the intrinsic charge and discharge capacity performance of the battery. Accordingly, the second capacity can be regarded as a suitable reference value. The discharge capacities of the pristine MoS_2, CM, CMC (unannealed), and CMC (annealed) after 100 cycles were 27, 144.8, 200.4, and 422.46 mAh g^{-1}, respectively. In comparison to pristine MoS_2, the CM synthesized doped with cerium exhibits a favorable specific capacity. Following the addition of carbon materials, the initial capacity is not as high as that of CM. However, the material demonstrates a notable enhancement in cyclic stability. After annealing, the CMC composite displays the most favorable cyclic stability. The incorporation of Ce elements can reduce the rate of capacity decay and enhance cycling performance, thereby extending the operational lifespan of the battery. CMC composites were synthesized through the doping of C elements, resulting in enhanced conductivity and optimized electron transport.[16,29]

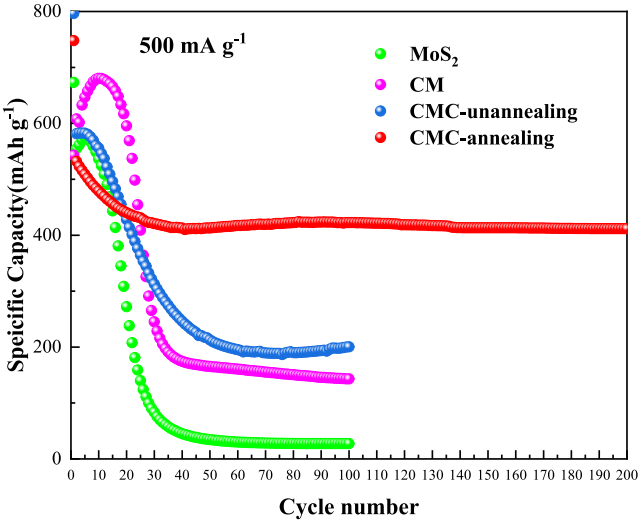

Figure 8. Cyclic stability of MoS_2, CM, CMC, and CMC after annealing.

Furthermore, the incorporation of carbon materials enhanced the crystallinity of the material, as illustrated by the XRD patterns in Figure 3. The uniform distribution of C into the CM enhanced the stability of the material and reduced capacity decay during the cycle, thereby improving the cyclic stability of the material. The capacity retention rate of CMC after annealing at 500 °C is 77.34%. Table 2 presents the electrochemical performance of various MoS_2-based anode materials synthesized through disparate methodologies.

To investigate the cycling stability of composite materials, the batteries were disassembled after cycling, and field emission scanning electron microscopy (FESEM) observations were promptly conducted on the anode slices. Figure 9a,b depicts the morphologies of the anode slices after annealing CMC cycling for 5 and 100 cycles, respectively. Figure 9c shows the anode slice after cycling 100 times without annealing the CMC. After 5 cycles, a complete layer film has grown on the anode slice. Following 100 cycles, the film was observed to vanish in certain areas. In contrast, for the anode slices prepared with CMC and subjected to 100 cycles, large areas of voids appear on the film grown on the surface of the slices, accompanied by the disappearance of the film. This indicates a significant collapse of the composite material. By comparison, it is found that the CMC composite material exhibits an enhanced cycling stability after annealing.

Figure 10a,b presents the cyclic voltammetry (CV) curves of the CMC composite electrodes before and after annealing at 500 °C for 2 h. As illustrated in Figure 10a, the CMC electrodes without annealing show two reduction peaks in the first cathodic scanning. The weak peak at 1.4 V is attributed to the formation of amorphous Li_xMoS_2, which is a result of Li^+ embedding within the molybdenum disulfide lattice, as indicated. Moreover, the reduction peak at 0.4 V can be assigned to the conversion of Li_xMoS_2 to Li_2S. The reaction between lithium ions and electrolytes results in the formation of a solid electrolyte interface (SEI) film. After annealing, the two reduction peaks shift to 1.3 and 0.45 V, respectively, during the initial cathodic scan. As for anode scanning, the CMC electrodes before annealing exhibit two distinct

Table 2. Cyclic Stability of the MoS_2-Based Anode Synthesized by Different Methods

material	morphology	method	time	initial discharge-specific capacity	capacity retention (Nth) (mAh g^{-1})	references
$Ce_2Mo_3O_{12}/MoS_2/C$	nanoflower	hydrothermal	8 h	747.98 mAh g^{-1} (0.5 A g^{-1})	411.6 (200th)	this work
MoS_2/MXene	nanosheet	hydrothermal	12 h	738 mAh g^{-1} (0.1 A g^{-1})	731 (100th)	1
MoS_2	layered structure	hydrothermal	6 h	(0.05 A g^{-1})	108 (500th)	53
MoS_2/TiO_2	micrometer florid	hydrothermal	16 h	410.8 mAh g^{-1} (0.8 A g^{-1})	361.5 (300th)	18
MoS_2	nanoflower	hydrothermal	24 h	(1 C)	430 (300th)	7
CoS_2/MoS_2	nanosphere	solvothermal	2 h	(0.2 A g^{-1})	319.2 (100th)	8
MoS_2	nanosheets	hydrothermal	24 h	501 mAh g^{-1} (1 A g^{-1})	142 (600th)	54
Sn-MoS_2		vacancy-assisted compositing	16 h	1260 mAh g^{-1} (1 A g^{-1})	160 (100th)	55

https://doi.org/10.1021/acsomega.4c11155
ACS Omega 2025, 10, 18539−18551

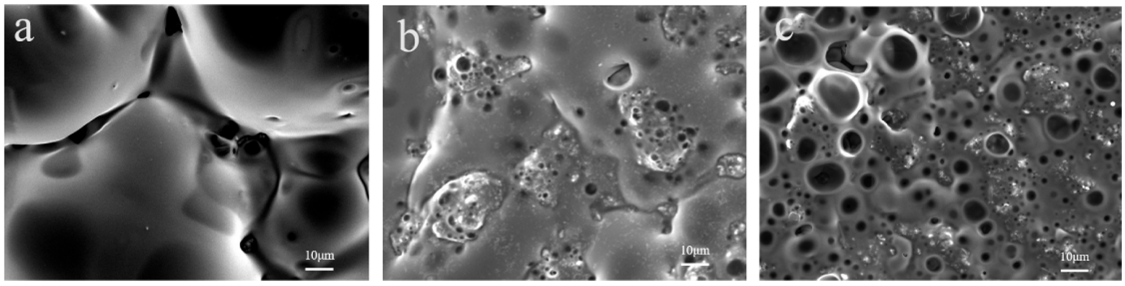

Figure 9. FESEM images of the anode slices after annealing CMC cycling for 5 cycles (a) and 100 cycles (b) CM, the anode slices CMC cycling for 100 cycles (c).

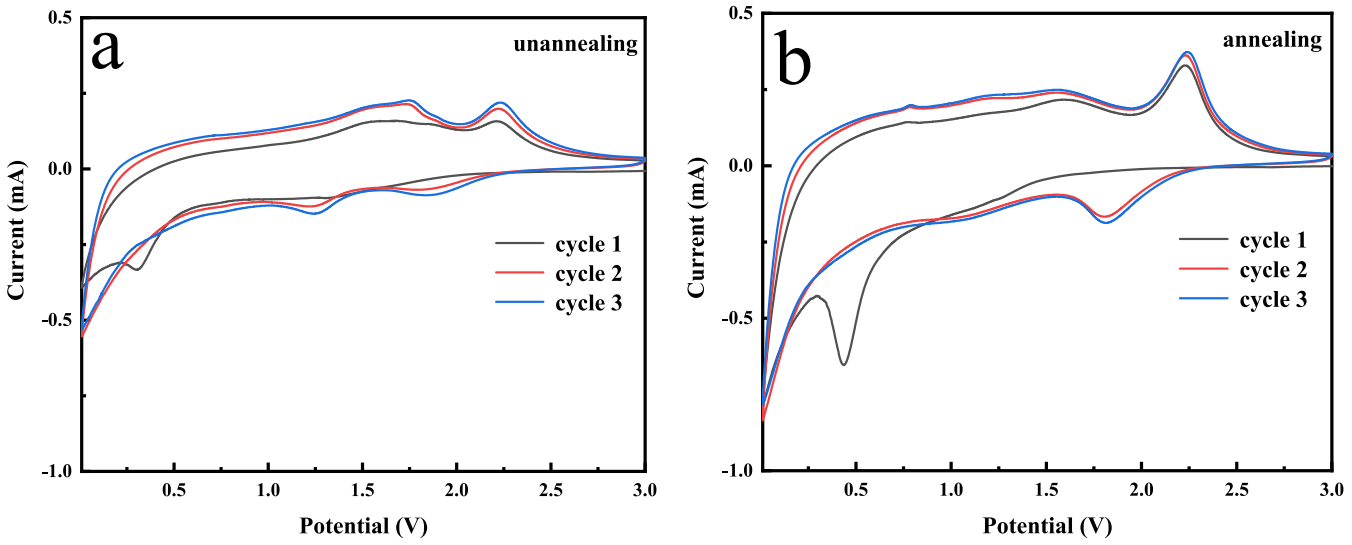

Figure 10. CV curves for the first three cycles of CMC electrode (a) and CMC electrode after annealing (b) at the scanning rate of 0.3 mV/S, with the voltage range from 0.01 to 3 V.

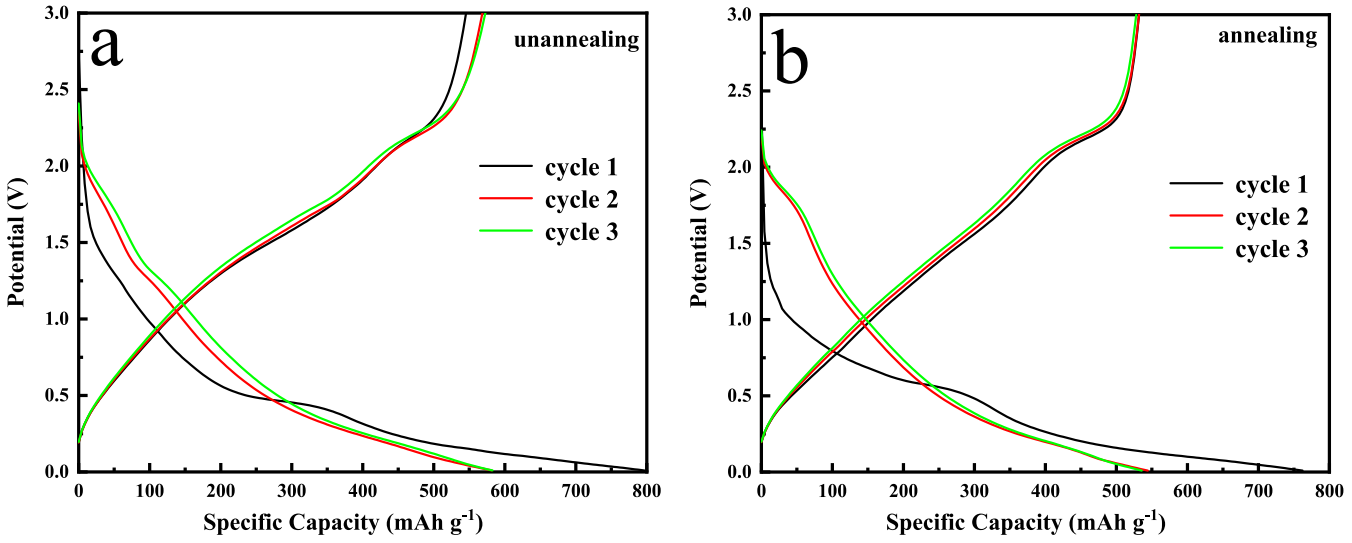

Figure 11. Charge and discharge curves of CMC (a) and CMC after annealing (b) at 500 °C.

oxidation peaks at approximately 1.75 and 2.15 V, respectively (as shown in Figure 10a). The peak at 1.75 V corresponds to the conversion of Li_2S to S. Moreover, the peak at 2.15 V can be due to the partial vulcanization of Mo to form MoS_2. After annealing, the oxidation peaks of the composite electrode exhibit a shift to approximately 1.65 and 2.25 V. As per the CV curves of the CMC composite electrodes before and after annealing, there is no significant difference in the peak positions, suggesting that the electrochemical reactions occurring during the charge and discharge cycles are identical. The high coincidence of CV curves in the following two cycles indicates that the CMC composite exhibits excellent cycle stability both before and after annealing, as observed in previous cycles.[11,14,56]

https://doi.org/10.1021/acsomega.4c11155
ACS Omega 2025, 10, 18539−18551

Figure 11a,b illustrates the charge−discharge profiles of the CMC composite during the initial three cycles within a voltage range of 0.01 to 3 V at a current density of 500 mA g^{-1}. The specific discharge capacities of the CMC composite before and after annealing during the first cycle are 796.4 and 762.1 mAh g^{-1}, respectively. However, the capacities after the first cycle decrease in the subsequent two cycles. The loss of capacity is mainly associated with the formation of the SEI film. The perfectly superimposed curves in the second and third cycles demonstrate the favorable reversibility and cycle stability of the CMC composite as an anode material. Two different plateaus at 1.5 and 0.4 V are shown in the charging curves for samples with the CMC composite electrodes before annealing. After annealing, two discharge platforms emerge at approximately 1.1 and 0.5 V. The voltage platforms at 1.5 and 1.1 V correspond to the insertion of Li^+ between the MoS_2 layers to form the intercalation compound Li_xMoS_2. The observed voltage platforms at 0.4 and 0.5 V indicate that the intercalation compound experiences a transformation into Mo nanoparticles and Li_2S. The CMC materials after annealing display a disparate discharge potential plateau during the second and third cycles in comparison to the first cycle. This indicates that an irreversible reaction occurred, resulting in the formation of Li_xMoS_2.

Figure 12 presents a comparison of the rate capabilities of CMC samples before and after annealing. The rate performance of the CMC electrode before annealing exhibited reversible capacities of 623.0, 512.6, 328.2, and 180.6 mAh g^{-1} at current densities of 0.1, 0.2, 0.5, and 1 A g^{-1}, respectively. When the current density returns to 0.1 A g^{-1}, the reversible specific capacity recovers to 422.1 mAh g^{-1}, indicating poor rate performance. During the rate capability testing of lithium-ion half-cells, the specific capacity of the battery continues to decline as the current density increases. The intercalation-deintercalation process of lithium ions within electrode materials necessitates a certain amount of time. When the current density increases, the number of Li^+ ions required to migrate per unit time escalates, yet the diffusion rate intrinsic to the material remains limited. This leads to the under-utilization of some active materials. Additionally, the internal structure of the composite material can be disrupted at higher current densities, causing the specific capacity of the material to continue declining even after the current density returns to 0.1 A g^{-1}. The specific discharge capacities of the CMC electrode after annealing are 609.1, 536.3, 449.2, and 370.6 mAh g^{-1} at current densities of 0.1, 0.2, 0.5, and 1 A g^{-1}, respectively. When the current density is restored to 0.1 A g^{-1}, the specific capacity of the CMC electrode before annealing is 588.5 mAh g^{-1}, with a capacity retention rate of 96.6%. It can be observed that the CMC electrode after annealing exhibits a superior rate performance. This phenomenon can be attributed to the enhancement of the electrical conductivity of the active material resulting from the annealing procedure, which consequently leads to an augmented reversible capacity. The annealing treatment enhances the crystallinity of the material and mitigates the disruption of particles during the cycle process.

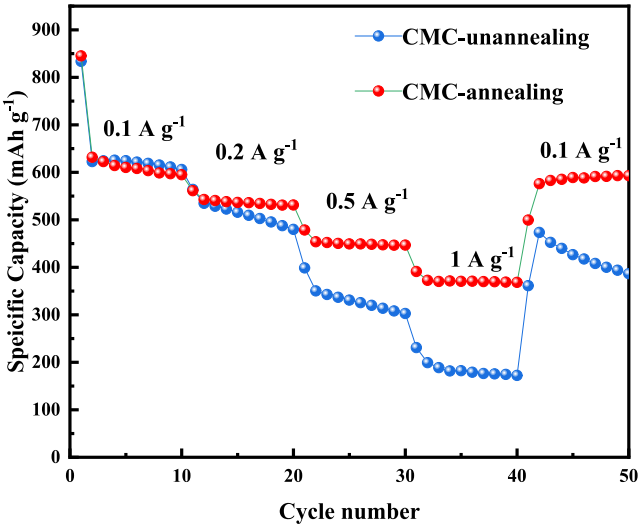

Figure 12. Rate performance of the CMC before and after annealing.

In order to investigate the kinetic process of the CMC electrode, electrochemical impedance spectroscopy (EIS) tests were performed. The equivalent circuit and the Nyquist diagram were fitted by using Zview, as illustrated in Figure 13.

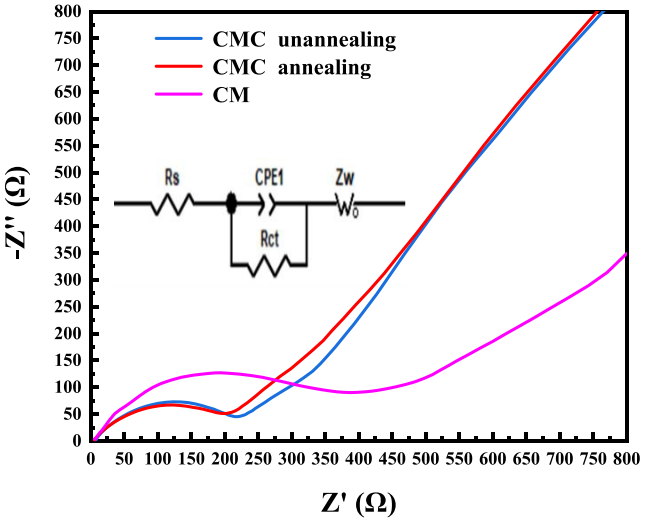

Figure 13. Electrochemical impedance spectra (EIS) and equivalent circuit diagram of the CMC electrode.

R_s represents the internal resistance of the cell, which is attributed to the combined physical and contact resistances within the lithium-ion battery. It corresponds to the intercept from zero to the starting point of the semiarc on the Z' axis. The charge transfer resistance at the electrode−electrolyte interface, designated as R_{ct}, reflects the electrochemical properties of the active material. It corresponds to the intercept of the semiarc of the high-frequency region on the Z' axis. Additionally, Z_w represents Warburg impedance, which signifies the diffusion resistance of Li^+ in the electrolyte. This is represented by the intercept of the slash line in the low-frequency region on the Z′ axis. The CPE represents the corresponding constant phase element.[57−59] As illustrated in the impedance diagram, the introduction of carbon dramatically reduced the resistance of the composite electrode. The resistance of the CM electrode is 375 Ω, whereas the resistance of the CMC electrode incorporated with C is 212 Ω. This suggests that the incorporation of carbon significantly diminishes the charge transfer impedance and enhances the electrical conductivity of the material, thereby enhancing its charge transport performance.[11,41,60] Furthermore, upon

https://doi.org/10.1021/acsomega.4c11155
ACS Omega 2025, 10, 18539−18551

annealing at 500 °C, the charge transfer resistance (R_{ct}) value of the CMC composite decreased to 202 Ω, representing the lowest value observed among the specimens. These findings indicate that the annealed CMC composite exhibits superior charge transport and lithium-ion diffusion properties during the charge/discharge cycles. This suggests that an annealing treatment may be an effective method for further reducing the R_{ct} of the composite electrode.[61] Specifically, the CMC electrode after annealing exhibits increased conductivity and a significantly enhanced electrochemical performance.

4. CONCLUSIONS

In summary, nanoflower-like CMC composite powder was prepared by using an enhanced hydrothermal method. The as-synthesized CMC composite exhibits a nanoflower-like structure formed by the aggregation of nanosheets. Annealing has little effect on the morphology of the prepared CMC sample. In comparison to pristine MoS_2, the CM composite synthesis doped with Ce exhibits a favorable cycle stability. Following the addition of carbon materials, while the initial capacity is not as high as that of CM, the material cycle stability demonstrates a notable enhancement. After annealing, the CMC material displayed the most favorable cyclic stability. After annealing at 500 °C, the CMC composite exhibited remarkable cycle stability as an anode material for lithium-ion batteries. The initial discharge capacity at a current density of 500 mA g^{-1} was 747.98 mAh g^{-1}, while the discharge capacity after 200 cycles exhibited a capacity retention rate of 77.34%. It is anticipated that this study will provide a potential approach for the rational design of related materials.

AUTHOR INFORMATION

Corresponding Author

Wei Liu − *School of Material Science and Engineering, Henan University of Science and Technology, Luoyang 471003, China; Collaborative Innovation Center for New Materials and Advanced Processing Technologies of Nonferrous Metals, Luoyang 471003, China;* orcid.org/0009-0003-0773-201X; Email: liuwei@haust.edu.cn

Authors

Jingbo Zhang − *School of Material Science and Engineering, Henan University of Science and Technology, Luoyang 471003, China; Henan University of Science and Technology National Joint Engineering Research Center for Abrasion Control and Molding of Metal Materials, Luoyang 471023, China*

Dongsheng Fan − *School of Material Science and Engineering, Henan University of Science and Technology, Luoyang 471003, China; Henan University of Science and Technology National Joint Engineering Research Center for Abrasion Control and Molding of Metal Materials, Luoyang 471023, China*

Yaozong Lu − *School of Material Science and Engineering, Henan University of Science and Technology, Luoyang 471003, China; Henan University of Science and Technology National Joint Engineering Research Center for Abrasion Control and Molding of Metal Materials, Luoyang 471023, China*

Linping Fu − *School of Material Science and Engineering, Henan University of Science and Technology, Luoyang 471003, China; Henan University of Science and Technology National Joint Engineering Research Center for Abrasion Control and Molding of Metal Materials, Luoyang 471023, China*

Longhua Zhang − *School of Material Science and Engineering, Henan University of Science and Technology, Luoyang 471003, China*

Ming Li − *School of Material Science and Engineering, Henan University of Science and Technology, Luoyang 471003, China*

Complete contact information is available at: https://pubs.acs.org/10.1021/acsomega.4c11155

Notes

The authors declare no competing financial interest.

ACKNOWLEDGMENTS

This research was financially supported by the National Natural Science Foundation of China (grant no. U1404511), the Henan Province Science and Technology R&D Program Joint Fund Project (grant no. 222103810038), Student Research Training Program of Henan University of Science and Technology (No. 2024049), and the Henan Provincial University Key Research Project (grant no. 24B430007).

REFERENCES

(1) Gong, C.; Long, M.; Xiao, J.; Li, J.; Chen, J.; Xiao, Y.; Zhang, G.; Gao, H.; Liu, H. One-Step Hydrothermal Reaction Induced Nitrogen-Doped MoS_2/MXene Composites with Superior Lithium-Ion Storage. *Batteries* **2022**, *8* (10), 156.

(2) Arshad, F.; Lin, J.; Manurkar, N.; Fan, E.; Ahmad, A.; Tariq, M. u. N.; Wu, F.; Chen, R.; Li, L. Life cycle assessment of lithium-ion batteries: a critical review. *Resour., Conserv. Recycl.* **2022**, *180*, No. 106164.

(3) Zhao, G.; Cheng, Y.; Sun, P.; Ma, W.; Hao, S.; Wang, X.; Liu, M.; et al. Biocarbon based template synthesis of uniform lamellar MoS_2 nanoflowers with excellent energy storage performance in lithium-ion battery and supercapacitors. *Electrochim. Acta* **2020**, *331*, No. 135262.

(4) Jia, P.; Liang, J.; Yue, L.; Liu, M.; Wang, X.; Liang, C.; Yu, K. Effect of MoS_2 decoration on energy storage of wheat straw-derived porous carbon for lithium-ion batteries. *Ionics* **2023**, *29* (12), 5085−5097.

(5) Jiang, J.; Zhang, Y.; An, Y.; Wu, L.; Zhu, Q.; Dou, H.; Zhang, X. Engineering ultrathin MoS_2 nanosheets anchored on N-doped carbon microspheres with pseudocapacitive properties for high-performance lithium-ion capacitors. *Small Methods* **2019**, *3* (7), No. 1900081.

(6) Liu, B.; Li, F.; Li, H.; Zhang, S.; Liu, J.; He, X.; Jia, X.; et al. Monodisperse MoS_2/graphite composite anode materials for advanced lithium ion batteries. *Molecules* **2023**, *28* (6), 2775.

(7) Liu, M.; Li, N.; Wang, S.; Li, Y.; Liang, C.; Yu, K. 3D nanoflower-like MoS_2 grown on wheat straw cellulose carbon for lithium-ion battery anode material. *J. Alloys Compd.* **2023**, *933*, No. 167689.

(8) Zhang, Q.; Yao, T.; He, Q.; Wang, H.; Liu, Z.; Wang, D.; Wang, H.; Meng, L. Enhancing lithium-ion storage performance of hollow CoS_2/MoS_2 nanospheres via N-doped carbon-coating. *J. Energy Storage* **2023**, *72*, No. 108639.

(9) Xu, H.; Jiang, C.; Ye, W.; Xiong, D.; Chen, L.; Feng, Z.; He, M.; et al. MoO_2-MoS_2 composite coated with polyaniline as an anode material for high-performance lithium ion batteries. *Ionics* **2024**, *30* (1), 85−94.

(10) Joseph, N.; Shafi, P. M.; Bose, A. C. Recent advances in 2D-MoS_2 and its composite nanostructures for supercapacitor electrode application. *Energy Fuels* **2020**, *34* (6), 6558−6597.

(11) Liu, Y.; Cui, C.; Liu, Y.; Liu, W.; Wei, J. Application of MoS_2 in the cathode of lithium sulfur batteries. *RSC Adv.* **2020**, *10* (13), 7384−7395.

(12) Chang, K.; Chen, W.; Ma, L.; Li, H.; Li, H.; Huang, F.; Lee, J. Y.; et al. Graphene-like MoS_2/amorphous carbon composites with high capacity and excellent stability as anode materials for lithium ion batteries. *J. Mater. Chem.* **2011**, *21* (17), 6251−6257.
(13) Cao, R.; Chen, Y.; Ge, X.; Yuan, G.; Huang, T.; Xu, Q.; Wang, Z. Free-standing MoS_2/graphene flexible film as binder-free electrode for enhanced electrochemical performances in lithium-ion half-cells and full-cells. *Ionics* **2022**, *28*, 201−212.
(14) Bai, J.; Zhao, B.; Wang, X.; Ma, H.; Li, K.; Fang, Z.; Sun, Y.; et al. Yarn ball-like MoS_2 nanospheres coated by nitrogen-doped carbon for enhanced lithium and sodium storage performance. *J. Power Sources* **2020**, *465*, No. 228282.
(15) Liu, H.; Lin, Y.; Zhang, L. Hierarchical Porous MoS_2/C Nanospheres Self-Assembled by Nanosheets with High Electrochemical Energy Storage Performance. *Nanoscale Res. Lett.* **2020**, *15*, 199.
(16) Liu, W.; Fan, D.; Wang, W.; Yang, S.; Lu, Y.; Fu, L.; Zhang, J.; Wu, Y. One-Pot Hydrothermal Synthesis and Electrochemical Performance of Subspheroidal Core−Shell Structure MoS2/C Composite as Anode Material for Lithium-Ion Batteries. *Energies* **2024**, *17* (7), 1678.
(17) Chen, C.; Xie, X.; Anasori, B.; Sarycheva, A.; Makaryan, T.; Zhao, M.; Gogotsi, Y.; et al. MoS_2-on-MXene heterostructures as highly reversible anode materials for lithium-ion batteries. *Angew. Chem., Int. Ed.* **2018**, *57* (7), 1846−1850.
(18) Zhang, Y.; Zhao, S.; Zeng, X.; Xiao, J.; Dong, P.; Zhao, J.; Li, X. TiO_2−MoS_2 hybrid nano composites with 3D network architecture as binder-free flexible electrodes for lithium ion batteries. *J. Mater. Sci.: Mater. Electron.* **2017**, *28*, 9519−9527.
(19) Ghogare, T. T.; Pujari, R. B.; Lokhande, A. C.; Lokhande, C. D. Hydrothermal synthesis of nanostructured β-LaS_2 thin films. *Appl. Phys. A* **2018**, *124* (3), No. 248.
(20) Pujari, R. B.; Lokhande, A. C.; Ghogare, T. T.; Kale, S. B.; Lokhande, C. D. Hydrothermally synthesized monoclinic Yb_2S_3 thin films for supercapacitive application. *J. Mater. Sci.: Mater. Electron.* **2018**, *29*, 14116−14121.
(21) Wang, J.; Wang, Z.; Li, Y.; Ke, D.; Lin, X.; Han, S.; Ma, M. Effect of nano-sized Ce_2S_3 on reversible hydrogen storage properties of $LiBH_4$. *Int. J. Hydrogen Energy* **2016**, *41* (30), 13156−13162.
(22) Cheng, C.; Chen, F.; Yi, H.; Lai, G. CeO_2 mesoporous microspheres for high performance supercapacitors and lithium-ion batteries. *J. Energy Storage* **2021**, *35*, No. 102305.
(23) Wen, G.; Zhang, X.; Wang, J.; Wang, Y.; Rao, K.; Sui, Y.; Wu, L.; et al. Incorporating cerium dioxide into nitrogen-doped carbon fibers for high-performance lithium-ion batteries. *Adv. Powder Technol.* **2024**, *35* (4), No. 104384.
(24) Minakshi, M.; Mitchell, D. R.; Carter, M. L.; Appadoo, D.; Nallathamby, K. Microstructural and spectroscopic investigations into the effect of CeO_2 additions on the performance of a MnO_2 aqueous rechargeable battery. *Electrochim. Acta* **2009**, *54* (12), 3244−3249.
(25) Santhoshkumar, P.; Vikraman, D.; Hussain, S.; Karuppasamy, K.; Kathalingam, A.; Kim, H. S. 3D-architectured spherical $Ce_2Mo_5O_{16}$ by a time-dependent hydrothermal process and their energy storage application. *J. Alloys Compd.* **2022**, *928*, No. 167215.
(26) Feng, W.; Yang, H.; Pu, Z.; Zhang, L. Study of CNTs-MoS_2/CeO_2 composites for lithium-sulfur battery performance. *Ionics* **2022**, *28* (6), 2781−2791.
(27) Hou, B.; Wang, X.; Yao, J.; Zhang, H.; Yu, W.; Liu, G.; Wang, J. Fabrication of Ce_2S_3/MoS_2 composites via recrystallization-sulfurization method and their improved electrochemical performance for lithium-ion batteries. *J. Mater. Sci.: Mater. Electron.* **2017**, *28*, 12297−12305.
(28) Hou, B.; Wang, X.; Wang, J.; Yao, J.; Zhang, H.; Yu, W.; Wang, L.; et al. In situ synthesis of homogeneous Ce_2S_3/MoS_2 composites and their electrochemical performance for lithium ion batteries. *RSC Adv.* **2017**, *7* (11), 6309−6314.
(29) Liu, W.; Yang, S.; Fan, D.; Wu, Y.; Zhang, J.; Lu, Y.; Fu, L. Peg−Pvp-Assisted Hydrothermal Synthesis and Electrochemical Performance of N-Doped MoS_2/C Composites as Anode Material for Lithium-Ion Batteries. *ACS Omega* **2024**, *9* (8), 9792−9802.
(30) Zhang, Y.; Wang, N.; Bai, Z. The progress of cobalt-based anode materials for lithium ion batteries and sodium ion batteries. *Appl. Sci.* **2020**, *10* (9), 3098.
(31) Wang, A.; Zheng, Z.; Wang, H.; Chen, Y.; Luo, C.; Liang, D.; Yan, K.; et al. 3D hierarchical H_2-reduced Mn-doped CeO_2 microflowers assembled from nanotubes as a high-performance Fenton-like photocatalyst for tetracycline antibiotics degradation. *Appl. Catal., B* **2020**, *277*, No. 119171.
(32) Feng, Z.; Zhang, M.; Ren, Q.; Mo, S.; Peng, R.; Yan, D.; Ye, D.; et al. Design of 3-dimensionally self-assembled CeO_2 hierarchical nanosphere as high efficiency catalysts for toluene oxidation. *Chem. Eng. J.* **2019**, *369*, 18−25.
(33) Xu, F.; Meng, K.; Cao, S.; Jiang, C.; Chen, T.; Xu, J.; Yu, J. Step-by-step mechanism insights into the TiO_2/Ce_2S_3 S-scheme photocatalyst for enhanced aniline production with water as a proton source. *ACS Catal.* **2022**, *12* (1), 164−172.
(34) She, W.; Qi, T.; Cui, M.; Yan, P.; Ng, S. W.; Li, W.; Li, G. High catalytic performance of a CeO_2-supported Ni catalyst for hydrogenation of nitroarenes, fabricated via coordination-assisted strategy. *ACS Appl. Mater. Interfaces* **2018**, *10* (17), 14698−14707.
(35) Huang, L.; Kong, X.; Chang, K.; Tao, X.; Wang, Y.; Yu, Z. $Ce_2(MoO_4)_3$ synthesized with oleylamine and oleic acid as additives for photocatalysis: effect of preparation method. *Photochem. Photobiol. Sci.* **2023**, *22* (1), 241−250.
(36) Du, X.; Jiang, D.; Chen, S.; Dai, L.; Zhou, L.; Hao, N.; Wang, K.; et al. CeO_2 nanocrystallines ensemble-on-nitrogen-doped graphene nanocomposites: one-pot, rapid synthesis and excellent electrocatalytic activity for enzymatic biosensing. *Biosens. Bioelectron.* **2017**, *89*, 681−688.
(37) Cheng, P.; Shi, L.; Li, W.; Fang, X.; Cao, D.; Zhao, Y.; Cao, P.; Liu, D.; He, D. Efficient Regulation of Polysulfides by MoS2/MoO3 Heterostructures for High-Performance Li-S Batteries. *Small* **2023**, *19* (16), No. 2206083.
(38) Rui, S.; Li, Z.; Meng, L.; Wang, Q.; Xu, J.; Zhao, Y.; Jia, Q.; Li, H.; Lu, S.; Zhang, Y. Citric acid and plasma treated MoS_2 for high-performance supercapacitors. *J. Mater. Chem. C* **2025**, *13* (2), 849−857.
(39) Long, L. N.; Bich, T. T. N. Hydrothermal-based controllable synthesis and structural-optical characterization of 2D-MoS_2/graphene nanocomposites for optoelectronic applications. *Opt. Mater.* **2024**, *156*, No. 115968.
(40) Niu, M.; Zhu, Z.; Mou, Z.; Kang, W. Yolk-shelled MoS_2/C@Void@C@MoS_2 nanospheres as a stable and high-rate anode in sodium/potassium ion batteries. *Chem. Commun.* **2024**, *60* (95), 14053−14056.
(41) Wang, X.; Tian, J.; Cheng, X.; Na, R.; Wang, D.; Shan, Z. Chitosan-induced synthesis of hierarchical flower ridge-like MoS_2/N-doped carbon composites with enhanced lithium storage. *ACS Appl. Mater. Interfaces* **2018**, *10* (42), 35953−35962.
(42) Li, Y.; Mao, H.; Zheng, C.; Wang, J.; Che, Z.; Wei, M. Compositing reduced graphene oxide with interlayer spacing enlarged MoS_2 for performance enhanced sodium-ion batteries. *J. Phys. Chem. Solids* **2020**, *136*, No. 109163.
(43) Qing, M.; Hao, Z.; Zhao, X.; Dong, Q.; He, Z.; Hong, W.; Li, R. Amorphous MoS_2/MoO_3 Nanosheets as High-Efficient Polysulfide Barrier in Li− S Batteries. *Batteries Supercaps* **2024**, *7* (8), No. e202400089.
(44) Wang, S.; Zhao, L.; Li, J.; Tian, X.; Wu, X.; Feng, L. High valence state of Ni and Mo synergism in NiS_2-MoS_2 hetero-nanorods catalyst with layered surface structure for urea electrocatalysis. *J. Energy Chem.* **2022**, *66*, 483−492.
(45) You, J.; Qi, P.; Jia, Z.; Wang, Y.; Wang, D.; Tian, L.; Qi, T. Facile preparation of peanut shell derivatives supported MoS2 nanosheets for hydrogen evolution reaction. *Catal. Commun.* **2023**, *179*, No. 106693.

https://doi.org/10.1021/acsomega.4c11155
ACS Omega 2025, 10, 18539−18551

(46) Hui, K.; Fu, J.; Liu, J.; Chen, Y.; Gao, X.; Gao, T.; Tang, M.; et al. Yolk−shell nanoarchitecture for stabilizing a Ce_2S_3 anode. *Carbon Energy* **2021**, *3* (5), 709−720.
(47) Luo, X.; Li, N.; Guo, X.; Wu, K. One-pot hydrothermal synthesis of MoS_2 anchored corncob-derived carbon nanospheres for use as a high-capacity anode for reversible Li-ion battery. *J. Solid State Chem.* **2021**, *296*, No. 122020.
(48) Ma, T.; Liu, X.; Sun, L.; Xu, Y.; Zheng, L.; Zhang, J. MoS_2 nanosheets@ N-carbon microtubes: A rational design of sheet-on-tube architecture for enhanced lithium storage performances. *Electrochim. Acta* **2019**, *293*, 432−438.
(49) Liu, S.; Jia, K.; Yang, J.; He, S.; Liu, Z.; Wang, X.; Qiu, J. Encapsulating flower-like MoS_2 nanosheets into interlayer of nitrogen-doped graphene for high-performance lithium-ion storage. *Chem. Eng. J.* **2023**, *475*, No. 146181.
(50) Feng, N.; Meng, R.; Zu, L.; Feng, Y.; Peng, C.; Huang, J.; Yang, J.; et al. A polymer-direct-intercalation strategy for MoS_2/carbon-derived heteroaerogels with ultrahigh pseudocapacitance. *Nat. Commun.* **2019**, *10*, No. 1372.
(51) Mahmood, Q.; Park, S. K.; Kwon, K. D.; Chang, S. J.; Hong, J. Y.; Shen, G.; Park, H. S.; et al. Transition from diffusion-controlled intercalation into extrinsically pseudocapacitive charge storage of MoS_2 by nanoscale heterostructuring. *Adv. Energy Mater.* **2016**, *6* (1), No. 1501115.
(52) Fan, D. Synthesis and Performance of Rare Earth Compounds/Molybdenum Disulfide Composite as Anode Materials, M.S. Thesis; School of Material Science and Engineering, Henan University of Science and Technology: Luoyang, China, 2024.
(53) Tian, H.; Yu, M.; Liu, X.; Qian, J.; Qian, W.; Chen, Z.; Wu, Z. Plant-cell oriented few-layer MoS_2/C as high performance anodes for lithium-ion batteries. *Electrochim. Acta* **2022**, *424*, No. 140685.
(54) Xin, D.; He, S.; Zhang, X.; Li, R.; Qiang, W.; Duan, S.; Xia, M.; et al. Nitrogen plasma-induced phase engineering and titanium carbide/carbon nanotubes dual conductive skeletons endow molybdenum disulfide with significantly improved lithium storage performance. *J. Colloid Interface Sci.* **2025**, *678*, 704−716.
(55) Song, J.; Li, Y.; Liu, Z.; Zhu, C.; Imtiaz, M.; Ling, X.; Zhu, S.; et al. Enhanced lithium storage for MoS_2-based composites via a vacancy-assisted method. *Appl. Surf. Sci.* **2020**, *515*, No. 146103.
(56) Su, Q.; Wang, S.; Feng, M.; Du, G.; Xu, B. Direct studies on the lithium-storage mechanism of molybdenum disulfide. *Sci. Rep.* **2017**, *7* (1), No. 7275.
(57) Zhou, J.; Qin, J.; Zhang, X.; Shi, C.; Liu, E.; Li, J.; Zhao, N.; He, C. 2D space-confined synthesis of few-layer MoS_2 anchored on carbon nanosheet for lithium-ion battery anode. *ACS Nano* **2015**, *9* (4), 3837−3848.
(58) Sun, W.; Hu, Z.; Wang, C.; Tao, Z.; Chou, S. L.; Kang, Y. M.; Liu, H. K. Effects of carbon content on the electrochemical performances of MoS_2−C nanocomposites for Li-ion batteries. *ACS Appl. Mater. Interfaces* **2016**, *8* (34), 22168−22174.
(59) Chang, K.; Chen, W. L-cysteine-assisted synthesis of layered MoS_2/graphene composites with excellent electrochemical performances for lithium ion batteries. *ACS Nano* **2011**, *5* (6), 4720−4728.
(60) Wang, T.; Xu, Z.; Yang, J.; Liu, X.; Cheng, Y.; Li, J.; Shen, X.; Huang, J. Tailoring MoS_2 Ultrathin Sheets Anchored on Graphene Flexible Supports for Superstable Lithium-Ion Battery Anodes. *Part. Part. Syst. Charact.* **2019**, *36* (9), No. 1900197.
(61) Zhao, J.; Ren, H.; Gu, C.; Guan, W.; Song, X.; Huang, J. Synthesis of hierarchical molybdenum disulfide microplates consisting of numerous crosslinked nanosheets for lithium-ion batteries. *J. Alloys Compd.* **2019**, *781*, 174−185.

https://doi.org/10.1021/acsomega.4c11155
ACS Omega 2025, 10, 18539−18551